Memory preservation in highly-connected quantum networks

Simone Ausilio[1, 2], Fausto Borgonovi[3], Giuseppe Luca Celardo[4],
Jorge Yago Malo[1, *], and Maria Luisa Chiofalo[1]

[1]*Dipartimento di Fisica "Enrico Fermi" and INFN, Università di Pisa, Pisa, Italy*
[2]*University of Birmingham, Edgbaston, Birmingham, UK*
[3]*Dipartimento di Matematica e Fisica, Università Cattolica del Sacro Cuore, Brescia, Italy*
[4]*Dipartimento di Fisica e Astronomia, Università di Firenze, Firenze, Italy*
[*]*jorge.yago@unipi.it*

March 10, 2025

Abstract

Complex quantum networks are powerful tools in the modeling of transport phenomena, particularly for biological systems, and enable the study of emergent entanglement structures or topology effects in of many-body quantum systems.

Here, we study the transport properties of a quantum network described by the paradigmatic XXZ Hamiltonian, with non-trivial graph connectivity and topology, and long-range interaction.

Adopting a combination of analytical and numerical methods to analyze the properties of increasingly complex architectures, we find that all-to-all connected regular network preserves over long times the memory of initially injected excitations, tracing it back to the system symmetries and the cooperative shielding. We then develop understanding of the conditions for this property to survive in quantum networks with either power-law node connectivity or complex, small-world type, architectures. Interestingly, we find that memory preserving effects occur also in sparse and more irregular graphs, though to a significantly lower degree.

We discuss the implications of these properties in biology-related problems, such as an application to Weber's law in neuroscience, and their implementation in specific quantum technologies via biomimicry.

1

1 Introduction

Dynamical processes in quantum networks are relevant for the engineering of quantum simulators and quantum computing platforms [1], for the investigation of biological media under driven-dissipative conditions [2–4], and to map complex, non-linear phenomena that do not require to be quantum via the novel approach called quantum-like paradigm [5–7]. Complex quantum networks are also becoming powerful tools for extracting relevant information from many-body quantum systems [8], such as emergent entanglement structures, topological instabilities, and self-similarity in quantum states, which may not be apparent by traditional methods [9–11].

The importance of quantum networks, regular or complex, is enhanced by their accurate and precise engineering in current experimental setups, constituting a predominant area of development for quantum simulators [12–14], with widely transversal applications since the first proposals for quantum analog models more than 20 years ago [1]. Importantly, the current degree of experimental tunability and microscopic understanding of these platforms, both in their coherent and dissipative couplings [15], has enabled the quantum simulation of models well beyond condensed matter physics [16] or quantum computing, ranging from fundamental physics and cosmology [17], metrology and sensing [18] or – most relevant to this work – quantum thermalization and chaos [19],[20] quantum chemistry [21, 22] and biology [23].

Indeed, the characterization of quantum networks dynamics under open quantum system conditions constitutes a paradigmatic testbed for understanding information processing and transport phenomena in complex media both quantum and classical [24], addressing fundamental questions in diverse contexts. These include quantum information theory [25] with transversal implications for models of quantum gravity [26, 27]; material science, in parallel with the experimental and technological development of solid-state nanodevices and cold atom technologies [28, 29]; biological media, where the role of coherent processes in out-of-equilibrium phenomena, though still debated [30], has been proven in general complex networks and biological examples [2, 24, 31–34]. In fact, in more recent years the study of dynamics in complex networks topologies evolved under paradigmatic Hamiltonians, has raised attention to effectively investigate chemistry and biology applications, by different strategies that can be classified under two main categories. One is a multiscale approach that combines the quantum-chemistry computation of microscopic interaction potentials with the quantum simulation of energy or excitation transport in quantum networks [21, 23, 32]. Another one consists in mapping the complex (classical) network into a quantum network, and exploiting the underlying superposition and entanglement at work to describe the system non-linearities [14].

The quantum transport properties of a given system are governed by a set of general properties, all of which can be implemented in current quantum technology platforms: (i) the connectivity graph or network topology [35, 36], where the role of quantum interference produces drastic differences between classical and quantum regimes [24]; (ii) the presence of external couplings in the form

of driving [37, 38], disorder [39–41] or dissipation [2, 42], and (iii) the coherent Hamiltonian parameters governing the static properties of the model, i.e. not just the transfer rates and interaction strengths, but also the range of such couplings [43–45] with the latter being one of our focuses. Technological development, particularly in ion traps [46] and cold gases [47–49], has allowed to explore conditions where individual quantum systems are accurately prepared to couple over large distances. The long-range nature of the interactions has been studied in detail and it is known to affect the static and dynamical properties of a quantum model [45]. As to the static properties, it has been revealed to enrich the interplay between length scales in the system [50–52], leading to non-additive energy contributions [53], novel phases of matter, and distinguished changes in known spin [45, 54, 55] or cold-atom systems [56–58] phase diagrams, than for the case of short-range interactions. As to the dynamical behavior [53, 59], long-range interactions lead to a diversity of interesting phenomena. These concern the occurrence of non-thermal topological steady states [60, 61], excitation propagation beyond the Lieb-Robinson picture [62–65], new behavior in the presence of disorder [66], dissipation [67], applications to quantum reservoir computing [68] or, essential for the current work, trapped dynamics due to interference in what has been denoted as cooperative shielding [69]. Long-range interactions have revealed to be crucial in preserving over long time both temporal and spatial memory of excitation quenches in a regular, all-to-all connected XXZ open quantum network: this model resulted from the quantum mapping of a classical neuronal complex system and demonstrated [5] to effectively describe the sense of number [70, 71], the very general ability of humans and many animals of non-cognitively counting with constant precision of about 20% up to a few hundred items in a given space or time region [70]. Given the paradigmatic nature of the XXZ model [72], this time-space memory preserving feature can be predicted to apply to a variety of physical systems, besides being relevant for the development of quantum technology devices.

Understanding the physical mechanism governing this memory-preserving property is therefore of primary importance, exploring the whole variability of transport conditions represented by (i)-(iii) above. To this aim, analytical descriptions are especially valuable in combination with information that can be extracted from quantum simulating the time and spectral signals of the network dynamical observables. In this work, we first provide complete analytical understanding of this phenomenon in regular XXZ quantum networks encompassing (i) with all-to-all connectivity and (ii), after adopting the language of cooperative shielding, where protected subspaces emerge in the evolution due to the system symmetries [69]. Then, we turn to (iii) and parametrize the extent to which this phenomenon survives in regular quantum networks with power-law varying interactions. We finally revert back to (i) and advance the understanding of this phenomenon in complex XXZ quantum networks, choosing the specific and paradigmatic example of small-world networks, after combining in the semi-analytical outcomes of the so-called cascade model with quantum simulation data. This systematic study sets the stage for a deeper exploration of information and transport processing in paradigmatic XXZ quantum (com-

plex) networks, and the possible presence of universal behavior, revealing some degree of order in disordered structures.

The article is organized as follows. In Section 2, we introduce the XXZ model, analyze its symmetry structure, and exploit the latter to identify the physical mechanism for time-space memory preservation of excitations, in the light of cooperative shielding. The analytics are performed by first studying the all-to-all connected regular XX network and then adding the z-axis anisotropy interaction perturbatively. In Section 3, we explore the same phenomena in all-to-all connected regular networks with power-law decaying interactions and, then, in highly-connected random networks. Finally, in Section 4, we discuss the relevance of our findings for the phenomenological description of complex systems, and the perspective research questions that our work opens up.

2 Symmetry and dynamics in all-to-all connected quantum networks via cooperative shielding

We begin by introducing the paradigmatic Heisenberg XXZ Hamiltonian we are interested in, with its relevant properties and symmetries. As schematized in Fig. 1(a), the XXZ Hamiltonian is given by:

$$
\begin{aligned}
\hat{\mathcal{H}} &= \sum_{(i,j)} \Big[J_{ij}(\hat{\mathcal{S}}_i^x \hat{\mathcal{S}}_j^x + \hat{\mathcal{S}}_i^y \hat{\mathcal{S}}_j^y) + \Delta_{ij} \hat{\mathcal{S}}_i^z \hat{\mathcal{S}}_j^z \Big] \\
&= \sum_{(i,j)} \Big[\frac{J_{ij}}{2}(\hat{\mathcal{S}}_i^+ \hat{\mathcal{S}}_j^- + \hat{\mathcal{S}}_i^- \hat{\mathcal{S}}_j^+) + \Delta_{ij} \hat{\mathcal{S}}_i^z \hat{\mathcal{S}}_j^z \Big],
\end{aligned}
\tag{1}
$$

where $\hat{\mathcal{S}}_i^{x,y,z}$ represents the local spin magnetization on site i along the given direction and $\hat{\mathcal{S}}_i^{\pm}$ represent the corresponding ladder operators for the local spin Hilbert space. The sum runs over all the edges (i,j) of a given graph G, representing the interactions between sites. Therefore, for each site the physical neighbors are given by the vertex neighbors on the graph (see Fig. 1(a)). Quasi-particles are excited in the system, in the form of spin states (e.g. up, red circles) in a background of opposite spins (e.g. down, blue circles); for simplicity, throughout the paper we will call such quasi-particles *excitations*, in the sense of a given number of spins up (along the z direction) in a background of spins down as initial state of our system. They couple and travel to connected sites via exchange interaction J_{ij} between spins i and j. Sites possessing a link between them are connected by the hopping amplitude Δ_{ij}, which modulates the excitation spatial propagation.

The XXZ model has been studied at length for regular graphs with remarkable differences in local and global observables depending on the degree of coupling [5, 14, 69, 72]. Here, we focus on the case of highly-connected networks and the important example of all-to-all exchange coupling for the spreading of one single (see Fig. 1(b)) and several (see Fig. 1(d)) excitations. In the all-to-all connected case, the interference pattern that emerges from the high connectivity
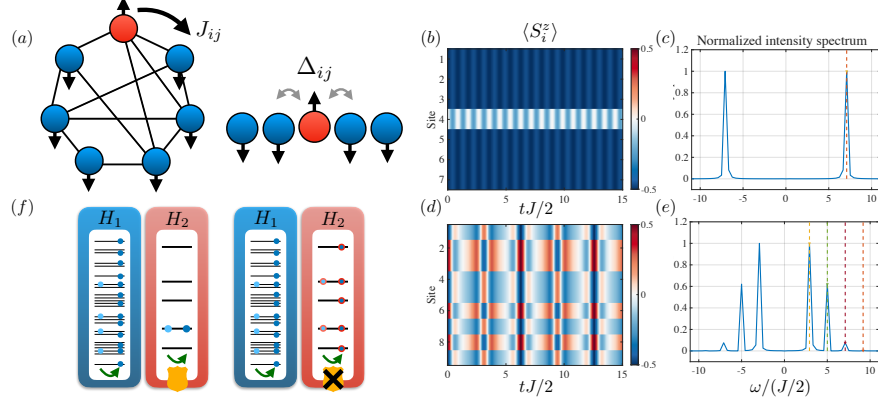
Figure 1: The concept. Cooperative shielding effects on the quantum network dynamics. (a) Quantum spin XXZ network. Excitations along the z-axis are depicted by red circles (spin up) in a background of non-excited blue circles (spin downs). The system presents two-body interactions by the spin-exchange coupling J_{ij} and the anisotropy Δ_{ij}. $(b) - (e)$ Temporal evolution of the local z-magnetization for the all-to-all connected XXZ spin network, revealing how the network preserves time and space memory of the excitations introduced over time, as a result of cooperative shielding (see (f)). (b) refers to a network with $L = 7$ sites and one excitation quench along x, i.e. with initial state $(|\downarrow\downarrow\downarrow\uparrow\downarrow\downarrow\downarrow\rangle + |\downarrow\downarrow\downarrow\downarrow\downarrow\downarrow\downarrow\rangle)/\sqrt{2}$ positioned at site 4; the arrows represent the spin direction along the z-axis. (d) refers to a network with $L = 9$ sites and four excitations quenches along z positioned at $i = 2, 3, 6, 8$, thus the initial state is $|\downarrow\uparrow\uparrow\downarrow\downarrow\uparrow\downarrow\uparrow\downarrow\rangle$. Example parameters chosen are $\Delta_{ij}=0$ and $J_{ij}/2 = 1$, dt=0.06 and periodic boundary conditions (PBC). Plots (c) and (e) depict the normalized power spectra of $\langle \hat{\mathcal{S}}_i^z \rangle$ in site $i = 4$ for cases (b) and (d) respectively, revealing how the number of peaks precisely reflects the number of excitations in the system, as a consequence of cooperative shielding: this is better explained in section 2.1. The data have been detrended before the Fourier transform removing the zero-frequency component. (f) How cooperative shielding works. Depiction of the energy spectra of two Hamiltonians $\hat{\mathcal{H}}_1$ and $\hat{\mathcal{H}}_2$, with light- and dark-blue dots referring to initial and time-evolved (green arrows) states under $\hat{\mathcal{H}} = \hat{\mathcal{H}}_1 + \hat{\mathcal{H}}_2$, respectively (see text for further details). Left panel: if the initial state belongs to an eigenspace of $\hat{\mathcal{H}}_2$ with eigenvalue λ_2 (only one level occupied), time only induces a global phase and the dynamics is determined only by $\hat{\mathcal{H}}_1$, thus protecting the eigenspace occupation (shield symbol) thanks to symmetry. Right panel: if the initial state extends to more than one eigenspace of $\hat{\mathcal{H}}_2$, the dynamics governed by $\hat{\mathcal{H}}$ allows for a delocalization of the state across multiple levels.

leads to substantial differences in the evolution, even at long times, compared to the familiar local models. The completely connected coupling induces high

symmetry and leads to a more interesting scenario, since the excitation goes back and forth from the earliest site to all the others in an evenly fashion. From a physical point of view, when the stimulus is located at the initial site i, it has equal probability to tunnel to any other node if $\Delta = 0$. Each pair of sites i and $j \neq i$ form what can be seen as an effective double-well potential problem, where the part of the excitation shared between that pair tunnels back and forth between the two potential minima. This, regular and symmetric, evolution becomes clear when analyzing the power spectrum of the time signal, Fig. $1(c)$ and (e), presenting a reduced set of discrete frequencies, as many as the initial excitations are, as we explain in section 2.1. Notice that when considering several excitations, while the time signal profile appears complex (Fig. $1(d)$), the power spectrum is still well-defined (Fig. $1(e)$).

Though apparently complicated, these observations can be traced back to an elegant symmetry argument, that we discuss below.

The role of symmetries in highly-connected graphs, Fig. $1(a)$, for integrable models has paramount importance to understand their quantum transport properties. Some of these dynamical phenomena have been studied in literature in what has been denoted as *cooperative shielding* [69]. This phenomenon appears in systems governed by a mean-field Hamiltonian and a long-range perturbation interaction between its constituents. It refers to the existence of protected subspaces within which the evolution remains unaffected for an extended duration due to the appearance of approximate selection rules, with the dynamics heavily depending on the initial state. We exemplify the concept in Fig. $1(f)$ for a simple situation. Let us consider a Hamiltonian $\hat{\mathcal{H}} = \hat{\mathcal{H}}_1 + \hat{\mathcal{H}}_2$ for a many-body system, having commuting parts $[\hat{\mathcal{H}}_1, \hat{\mathcal{H}}_2] = 0$. An initial state $|\psi_0\rangle$ belonging to a (degenerate or non-degenerate) eigenspace of $\hat{\mathcal{H}}_2$ and with corresponding eigenvalue λ_2, evolves in time according to the general Hamiltonian $|\psi(t)\rangle = \exp(-i\lambda_2 t)\exp(-i\hat{\mathcal{H}}_1 t)|\psi_0\rangle$: since $\hat{\mathcal{H}}_2$ solely induces a global phase without other effects, the dynamics is fully determined by $\hat{\mathcal{H}}_1$. On the contrary, if the initial state is disseminated across more than one eigenspace of $\hat{\mathcal{H}}_2$ its dynamics is characterized by $\hat{\mathcal{H}}$. This concept of trapping can be extended to the case of non-commuting Hamiltonian parts in the event of $\hat{\mathcal{H}}_2$ being composed of solely long-range interactions. If the initial state is initialized in a selected subspace of $\hat{\mathcal{H}}_2$, long-range interactions do not influence its temporal evolution for a time span that scales with the system size. Instead, the evolution of an initial state with components in more than one subspace, is affected by long-range interactions: the dynamics is not bounded, with components in various subspaces exhibiting fast propagation due to the long-range coupling.

With the cooperative shielding concept at hand, we now analyze in detail the consequences of the Hamiltonian symmetries on the energy levels and their effects on the dynamics. To this aim, we begin with the simplest case of the XX Hamiltonian, i.e. $\Delta_{ij} = 0$ in eq. (1), and then we turn it on again as a perturbation.

2.1 Eigenspaces of the exchange (XX) Hamiltonian

We start by analyzing only the exchange part of the Hamiltonian (1), and considering it as our unperturbed mean-field component: a similar treatment can be carried out for the Z part alone, still in the case of constant coupling between every couple of sites.

$$\hat{\mathcal{H}}_0 = J\sum_{i<j}(\hat{\mathcal{S}}_i^x\hat{\mathcal{S}}_j^x + \hat{\mathcal{S}}_i^y\hat{\mathcal{S}}_j^y) = \frac{J}{2}\sum_{i<j}(\hat{\mathcal{S}}_i^+\hat{\mathcal{S}}_j^- + \hat{\mathcal{S}}_i^-\hat{\mathcal{S}}_j^+)\,.$$

We show below that $\hat{\mathcal{H}}_0$ can be rewritten as function of the total z-magnetization $\hat{\mathcal{M}}_z = \sum_i \hat{\mathcal{S}}_i^z$ and of the (Casimir invariant) total squared magnetization $\hat{\mathcal{M}}^2 = \hat{\mathcal{M}}_x^2 + \hat{\mathcal{M}}_y^2 + \hat{\mathcal{M}}_z^2$, see [69]. We then re-cast the operators $\hat{\mathcal{S}}_i^x\hat{\mathcal{S}}_j^x$ (equivalent for the y-component) in terms of $\hat{\mathcal{M}}_z$ and $\hat{\mathcal{M}}^2$ as:

$$\hat{\mathcal{M}}_x^2 = \sum_k(\hat{\mathcal{S}}_k^x)^2 + 2\sum_{i<j}\hat{\mathcal{S}}_i^x\hat{\mathcal{S}}_j^x \Leftrightarrow \sum_{i<j}\hat{\mathcal{S}}_i^x\hat{\mathcal{S}}_j^x = \frac{\hat{\mathcal{M}}_x^2 - \sum_k(\hat{\mathcal{S}}_k^x)^2}{2}\,.$$

Additionally, we express each local spin operator as $(\hat{\mathcal{S}}_k^x)^2+(\hat{\mathcal{S}}_k^y)^2 = \hat{\mathcal{S}}_k^2-(\hat{\mathcal{S}}_k^z)^2 = 1/2(1/2+1)-(1/2)^2 = 1/2$, the action of these operators on the single particles being known. Thus, the Hamiltonian becomes:

$$\hat{\mathcal{H}}_0 = \frac{J}{4}\Big[2(\hat{\mathcal{M}}^2 - \hat{\mathcal{M}}_z^2) - L\Big], \tag{2}$$

with L the system size. For reference, the respective computation made for the Z part only amounts to $\hat{\mathcal{H}}_0' = J/2(\hat{\mathcal{M}}_z^2 - L/4)$. The result in Eq. (2) implies that although the starting Hamiltonian is the sum of two-body interacting terms, the all-to-all connectivity allows for the appearance of collective behavior, where the system behaves as if it had a single, large spin [73]. Labeling the quantum numbers associated to operators $\hat{\mathcal{M}}^2$ and $\hat{\mathcal{M}}_z$ with l and m, respectively, we use the angular momenta composition rules for spin-$1/2$ to calculate the corresponding energy bands E_{lm}:

$$l = \begin{cases} 0, 1, \ldots, \frac{L}{2} & \text{if } L \text{ is even} \\ \frac{1}{2}, \frac{3}{2}, \ldots, \frac{L}{2} & \text{if } L \text{ is odd} \end{cases}$$

$$m = -l, (-l+1), \ldots, (l-1), l \quad (2l+1 \text{ values})$$

$$E_{lm} = \frac{J}{4}\Big[2\Big(l(l+1) - m^2\Big) - L\Big]. \tag{3}$$

The degeneracy $f(l, L)$ of a certain value of l for a given L, can be computed recursively with:

$$\begin{cases} f\left(\frac{1}{2}, 1\right) = 1\,; \\ f(l \text{ not allowed}, L) = 0\,; \\ f(l, L) = f\left(l - \frac{1}{2}, L-1\right) + f\left(l + \frac{1}{2}, L-1\right). \end{cases}$$
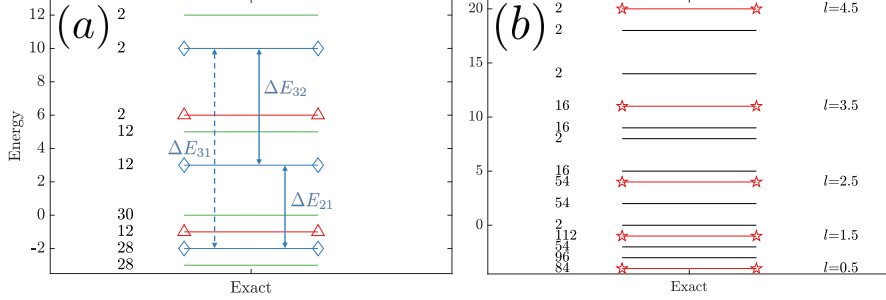
Figure 2: Symmetries and structure of the energy levels for the all-to-all connected XX Hamiltonian. (a) Diagram for a system with $L = 7$ sites and constant exchange coupling $J/2 = 1$ (unperturbed study). The vertical axis represents the exact values of the eigenvalues of $\hat{\mathcal{H}}_0$, while the numbers on the left of the horizontal lines account for the degeneracy of the corresponding level; different colors and symbols represent different subspaces corresponding to different number of excitations along the z-axis. Red triangles and lines: levels corresponding to 1 excitation. Blue lozenges and lines: levels referring to 2 excitations. Double-headed arrows : the three possible energy gaps described by Eq. (5): the dotted arrow represents the frequency that is not manifested in the z-magnetization spectrum. Green bars: remaining energy levels. (b) The same diagram for the case $L = 9$, with the red bars contoured by stars representing the levels with 4 excitations denoted by the quantum number l on the right.

The Hamiltonian $\mathbb{Z}_2$ symmetry also implies that $E_{l,m} = E_{l,-m}$. Hence, the level degeneracy is:

$$\deg(E_{l|m|}, L) = \begin{cases} 2f(l, L) & \text{if } L \text{ is odd or } L \text{ is even and } m \neq 0 \\ f(l, L) & \text{if } L \text{ is even and } m = 0 \end{cases} .$$

We depict in Fig. 2 the energies and degeneracies of the all-to-all graph, highlighting the energy levels belonging to the subspaces that correspond to one (triangles) and two (diamonds) spins up. They spread across two and three energy bands, respectively, as it is dictated by the possible choices of the quantum number l.

We are now in a position to explain the local z-magnetization spectra in Fig. 1 in terms of the energy levels. Due to the $U(1)$ symmetry, the quantum number m will be fixed during the time evolution. If we consider the case of one single excitation to start with, we have $m_1 = (-L/2) + 1$, hence only the values $l_1 = (L/2) - 1$ and $l_2 = L/2$ are allowed, the corresponding bands having energies $E_{l_1 m_1} = -J/2 \doteq E_1^{(1)}$ with degeneracy $L - 1$ and $E_{l_2 m_1} = J(L - 1)/2 \doteq E_2^{(1)}$ with degeneracy 1. Thus, the oscillation of the local z-magnetization signal

occurs at angular frequency equal to the energy split between the two levels:

$$\Delta E = E_2^{(1)} - E_1^{(1)} = \frac{JL}{2}\,. \tag{4}$$

We notice that the local z-magnetization spectra depend explicitly on the separation between the energy levels of the system.

We can use the same line of reasoning for the second case highlighted in Fig. 2(a), with two excitations. Here, the quantum number m is fixed to be $m_2 = (-L/2) + 2$, implying that l can take values $l_1 = (L/2) - 2$, $l_2 = (L/2) - 1$ and $l_3 = L/2$, reflecting in the energy levels as $E_{l_1 m_2} = -J \doteq E_1^{(2)}$ with degeneracy $L(L-3)/2$; $E_{l_2 m_2} = J(L-4)/2 \doteq E_2^{(2)}$ with degeneracy $L-1$; $E_{l_3 m_2} = J(L-2) \doteq E_3^{(3)}$ with degeneracy 1. The resulting energy gaps are:

$$\Delta E_{21}^{(2)} = E_2^{(2)} - E_1^{(2)} = \frac{J(L-2)}{2}\,;$$
$$\Delta E_{32}^{(2)} = E_3^{(2)} - E_2^{(2)} = \frac{JL}{2}\,;$$
$$\Delta E_{31}^{(2)} = E_3^{(2)} - E_1^{(2)} = \Delta E_{32}^{(2)} + \Delta E_{21}^{(2)} = J(L-1)\,. \tag{5}$$

Focusing on the case of two excitations, we analyze in Fig. 3 the power spectrum of the local magnetization $\langle \hat{\mathcal{S}}_v^z \rangle(t)$. In Fig. 3(a), we observe the presence of two frequencies, corresponding to the gaps ΔE_{21} and ΔE_{32}, while the third possible transition is absent. Even in the case depicted in Fig.1(d) $-$ (e), corresponding to four initial excitations or $m = -L/2 + 4$, we ascertain the presence of four out of the $4(4-1)/2 = 6$ possible frequencies arising from the five levels having quantum number $l = L/2, L/2-1, L/2-2, L/2-3, L/2-4$; again, these four frequencies are exactly those coming from the difference between contiguous levels. The schematics for this situation is shown in Fig. 2(b).

To understand why it is so, we consider that for any expectation value of an operator as function of time and with initial state $|\psi_0\rangle$ we can write:

$$\langle \hat{\mathcal{O}} \rangle(t) = \langle \psi_0 | e^{i\hat{\mathcal{H}}t} \hat{\mathcal{O}} e^{-i\hat{\mathcal{H}}t} | \psi_0 \rangle = \sum_{m,n} \underbrace{\langle \psi_0 | \phi_m \rangle \langle \phi_n | \psi_0 \rangle \langle \phi_m | \hat{\mathcal{O}} | \phi_n \rangle}_{d_{mn}} e^{-i\Delta E_{mn}t}, \tag{6}$$

where we have decomposed the initial state $|\psi_0\rangle$ temporal evolution in the Hamiltonian eigenbasis $\{|\phi_n\rangle\}$, with corresponding eigenvalues $\{E_n\}$ (the pedices here represent a generic quantum number). In our specific case, the eigenstates of the system Hamiltonian $\hat{\mathcal{H}}_0$ are those of the angular momentum $|l, m\rangle$, with l and m defined in Eq. 3, the initial state is a superposition of Pauli strings, and the operator $\hat{\mathcal{O}}$ is a local spin operator $\hat{\mathcal{S}}_i^z \doteq \hat{\mathcal{O}}_0^{(1)}$ at site i: this operator has the property of being the $q = 0$ component of a spherical tensor of rank $r = 1$, the other components being $\hat{\mathcal{O}}_{+1}^{(1)} = -c\hat{\mathcal{S}}_i^+$ and $\hat{\mathcal{O}}_{-1}^{(1)} = c\hat{\mathcal{S}}_i^-$ with c a positive constant. The coefficients $\langle \psi_0 | \phi_m \rangle = \langle \psi_0 | \alpha; l, m \rangle$ and $\langle \phi_n | \psi_0 \rangle = \langle \beta; l', m' | \psi_0 \rangle$ are the Clebsch-Gordan coefficients between the eigenbasis and the Pauli basis,

9

where α and β denote the system-specific quantum numbers not related to angular momentum. The matrix elements of $\hat{\mathcal{O}}_0^{(1)}$ can be expressed thanks to the Wigner-Eckart theorem [74] as:

$$\langle \phi_m | \hat{\mathcal{O}} | \phi_n \rangle = \langle \alpha; l, m | \hat{\mathcal{O}}_0^{(1)} | \beta; l', m' \rangle \propto \langle l, m | r = 1, q = 0; l', m' \rangle \langle \alpha; l || \hat{\mathbf{O}}^{(1)} || \beta; l' \rangle,$$

with the first term being a Clebsch-Gordan coefficient and the second the reduced matrix element for tensor $\hat{\mathbf{O}}^{(1)} = \left(\hat{\mathcal{O}}_{+1}^{(1)}, \hat{\mathcal{O}}_0^{(1)}, \hat{\mathcal{O}}_{-1}^{(1)} \right)$. Put it another way, the theorem states that operating with a rank-r spherical tensor with states possessing an angular momentum l is equivalent to studying the composition of two angular momenta, one with spin r and the other with spin l. This analogy allows to define selection rules for the Clebsch-Gordan coefficients, which for the case at study translate in:

$$\begin{cases} |l - r| \leq l' \leq l + r \Rightarrow \Delta l = 0, \pm 1 \\ m' = m + q \Rightarrow m' = m \end{cases} \tag{7}$$

In other words, the system symmetries (notably invariance by rotations) guarantees that the connected matrix elements are those separated by $\Delta l \leq 1$ (and same value of m).

This property leads to the following key result: given an initial state with b excitations, i.e. b spin-up spins oriented along z and so total magnetization $m = -L/2 + b$; this initial state has support exclusively on the $b+1$ eigenspaces $l = L/2, L/2 - 1, \ldots, L/2 - b$, thus, due the selection rules in Eq.(7), we can observe exactly b frequencies in the power spectrum of $\langle \hat{\mathcal{S}}_i^z \rangle$.

Furthermore, the selection rule $m' = m$, valid for $q = 0$, allows to distinguish between the different subspaces of the total z-magnetization $\hat{\mathcal{M}}_z$ in case where the initial state is a superposition of states belonging to diverse magnetization sectors, like in Fig. 1(b). Considering this example, the initial state lives among the levels $(l = L/2, m = -L/2), (l = L/2, m = -L/2 + 1), (l = L/2 - 1, m = -L/2 + 1)$; the described selection rule isolates the total z-magnetization sector between them, so that the frequencies originated from the mechanism above for $m = -L/2 + 1$ do not mix up with those arising from the subspace with $m = -L/2$, with this remaining true for more general situations.

As a further numerical demonstration, we dub d_{mn} the coefficients depending on the eigenbasis overlaps with the initial state and the operator's matrix elements. The weights on the different exponentials are given by the sums of the corresponding $|d_{mn}|^2$ coefficients. We show in Fig. 3(b) the numerical evaluation of the coefficients normalized to their total sum. We notice that the position of the two resulting finite frequencies perfectly matches that displayed in the numerically simulated power spectrum, Fig.3(a). In particular, we observe a zero weight for ΔE_{31}, in agreement with the absence of this frequency in the simulated spectrum. While the value of the frequencies depends on the system size L, we show in Fig. 3(c) that their number does not. In fact, the number of frequencies only depends on the number of initial excitations, as it
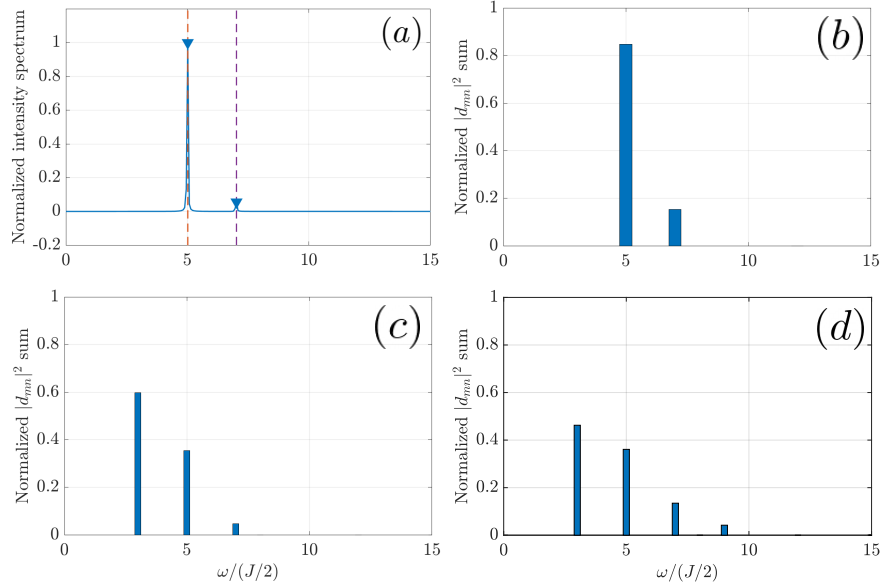
Figure 3: Multiple excitations with all-to-all connected XX network: frequency analysis. (a) Spectrum's peaks for the local z-magnetization signal in the case of two excitations: the corresponding positions are 5.02 ± 0.07 (higher prominence) and 7.02 ± 0.08 (lower prominence). The system parameters are the same as in Fig.1, with the signal being picked up from site 4. (b)$-$(d) Bar plot representing the distribution of the coefficients $|d_{mn}|^2$ in eq. (6), showing that the number of frequencies perfectly matches with the simulated spectra in Fig.1. As in the case of the spectra, the zero-frequency is not shown to highlight the oscillating components of the signals. The coefficients are summed over the levels' degeneracies and normalized to the total sum of the coefficients. (b) $L = 7$ and two excitations. (c) $L = 7$ and three excitations. (d) $L = 9$ and four excitations.

is visible in Fig. 3(d) for the case of 3 initial excitations, where one additional finite frequency adds on.

This analytical result embodies the physical interpretation of the simulational findings from [5, 14]: the all-to-all connected quantum network is capable of preserving long-lasting memory in space and time of the number of initially injected excitations, this memory being encoded in frequency spectrum of the collective spin excitations. To summarize, our analytical treatment evidences how the local z-magnetization spectra reveal the accessible gaps between consecutive energy levels, which in turn determine the number of excitations involved in the system. The accessible gaps are traced back to the Hamiltonian symmetry and their size enhanced by the all-to-all coupling condition, thereby favoring the protection of system subspaces according to the cooperative shielding concept. In simpler words, this outcome is linked to the collective behavior of the fully-

connected spin network with constant couplings, thus generating an effective, single large spin that blends together the single sites.

With this understanding at hand, we now proceed to analyze the effect of the anisotropy Z-term in Hamiltonian (1).

2.2 Role of the anisotropy (ZZ-term interaction)

Once the energy bands of the exchange Hamiltonian $\hat{\mathcal{H}}_0$ are computed, we can consider the effect of the anisotropy/interaction term in the Hamiltonian (1):

$$\hat{\mathcal{W}} = \sum_{i<j} \Delta_{ij} \hat{\mathcal{S}}_i^z \hat{\mathcal{S}}_j^z \, . \tag{8}$$

To this aim, we resort to perturbation theory and calculate to first order the energy shifts due to this contribution in Eq. (8).

Since the levels are degenerate, we should in principle compute (at first order) the eigenvalues of the $\hat{\mathcal{W}}$ perturbation restricted to the considered eigenspace. However, it can be easily checked by inspection that $\hat{\mathcal{W}}$ is already expressed in a diagonal form, due to the definitions of the Pauli basis $\mathcal{P}$. Therefore, we only need a restricted number of matrix elements. For any form of the Δ_{ij} coefficients one can cast the action of the perturbation operator on a given state in the computation basis $|\boldsymbol{\sigma}_q\rangle$, with $\boldsymbol{\sigma}_q$ expressing the spin polarizations vector in each site, the index q denoting the specific Pauli string. We thus obtain:

$$\langle \boldsymbol{\sigma}_q | \hat{\mathcal{W}} | \boldsymbol{\sigma}_q \rangle = \sum_{i<j} \Delta_{ij} \frac{\mathrm{sgn}(i,q)\mathrm{sgn}(j,q)}{4} \, , \tag{9}$$

where $\mathrm{sgn}(\cdot,\cdot)$ denotes the sign function. We can note how the shifts in energy depend on the pairwise products of the spins' directions in the basis vector. In order to simplify our analytical computation, we consider now nearest-neighbor interaction, in other words $\Delta_{ij} = \Delta_0$ if $\mathrm{dist}(i,j) = 1$ and vanishing otherwise. Under this condition, the energy shifts read:

$$\langle \boldsymbol{\sigma}_q | \hat{\mathcal{W}} | \boldsymbol{\sigma}_q \rangle = \frac{\Delta_0}{4} \sum_{i=1}^{L} \mathrm{sgn}(i,q)\mathrm{sgn}(i+1,q) \quad , \quad L+1 \equiv 1\,(\mathrm{PBC})\, . \tag{10}$$

For more general interactions, going back to Eq. (9), we consider the case of the first two neighbors having non-negligible interactions and with PBC:

$$\langle \boldsymbol{\sigma}_q | \hat{\mathcal{W}} | \boldsymbol{\sigma}_q \rangle = \frac{\Delta_1}{4} \sum_{i=1}^{L} \mathrm{sgn}(i,q)\mathrm{sgn}(i+1,q) + \frac{\Delta_2}{4} \sum_{i=1}^{L} \mathrm{sgn}(i,q)\mathrm{sgn}(i+2,q)\, ,$$

where Δ_1 and Δ_2 refer to the constant interaction coupling with the first and second neighbors, respectively.

Without loss of generality, we can hence turn to examine in detail the case of nearest-neighbor interaction for the perturbation. The shift reflects the fact that

if there is a total number of L couples (with PBC) and b is the number of pairs with opposite spin directions in a given Pauli string, the sum (10) corresponds to the number of consecutive pairs with spins pointing in the same direction after subtracting those with opposite spin, that amounts to $(L - b) - b = L - 2b$. By way of example, let us compare the resulting effect for the cases of one and two excitations. In the former case, there are only two out of the L couples of spins that have opposite directions. Thus, the summation in (10) amounts to $L - 4$ for each vector state of the restricted Pauli basis $\mathcal{P}_1$. This means that the shift is the same for both levels: importantly the perturbation has no overall effect on the local z-magnetization frequency. In the latter case, one can distinguish two possibilities for the Pauli strings, as depicted in table 1. According to the considered vector, one can get different values for the summation in eq. (10) and hence for the energy shift.

Excitation(s)	Sample Pauli string	Summation	Energy shift
1	↓↓↓↑↓↓↓	$L - 4$	$\Delta_0(L - 4)/4$
2 $(b = 2)$	↓↓↑↑↓↓↓	$L - 4$	$\Delta_0(L - 4)/4$
2 $(b = 4)$	↓↓↑↓↑↓↓	$L - 8$	$\Delta_0(L - 8)/4$
3 $(b = 2)$	↓↓↑↑↑↓↓	$L - 4$	$\Delta_0(L - 4)/4$
3 $(b = 4)$	↓↑↑↓↑↓↓	$L - 8$	$\Delta_0(L - 8)/4$
3 $(b = 6)$	↑↓↑↓↑↓↓	$L - 12$	$\Delta_0(L - 12)/4$

Table 1: Multiple excitations in all-to-all connected XXZ network. Examples of energy shifts computation for one, two, and three initial excitations (rows), with $0(1)$ denoting a spin up(down). First column: case at study. Second column: corresponding example of Pauli string. Third and fourth columns reveal the summation and the shift computed from eq. (10), respectively.

The present analysis can be generalized to an arbitrary number w of excitations. Reverting back to the Pauli strings examples appearing in Table 1, the largest shift is obtained when the configuration possesses the least amount of pairs with opposite spins, i.e. minimum number of domain walls: this implies $b = 2$ and $\delta E_{\max} = \Delta_0(L - 4)/4$. Instead, the smallest shift is obtained when all the excitations are separated, or in other words $b = 2w$ and $\delta E_{\min} = \Delta_0(L - 4w)/4$. Notice that we can now estimate the width of the band as the difference between the maximum and the minimum possible shifts, that is:

$$\delta E_{\max} - \delta E_{\min} = \frac{\Delta_0}{4}(L - 4 - L + 4w) = \Delta_0(w - 1). \tag{11}$$

We thus see that after introducing a given number of excitations, the maximum shift interval in (11) is proportional to the number of excitations in the

quantum spin network. As a result, the quantum network develops an uncertainty in the encoding of the number of excitations, that scales linearly with the number of excitations itself. The physical understanding of this network property is that the anisotropic interaction between nearest-neighbor spins shifts the original energy levels, thus creating enlarged spectrum from degeneracy breaking with further and wider peaks.

This result opens the door to applications in quantum technologies exploiting the memory-preserving property of the XXZ quantum network by engineering the ZZ anisotropy to obtain a constant relative uncertainty in the encoding of the number of excitations.

Interestingly, this result can also be linked to the description of information processing properties of the out-of-equilibrium XXZ network with all-to-all connectivity analyzed in [5, 14]. There, an ideal-observer analysis of the power spectra had shown that the uncertainty with which the quantum network encodes the number of frequency peaks - and therefore the number of excitations - linearly scales with the number itself. In neuroscience, this is the content of Weber's law describing the perception of the number of items in a space, or numerosity perception. This phenomenology is experimentally observed under very general conditions, no matter the perception channel (i.e. visual or auditory), nor the way the items are presented [70]. Importantly, neuroscience experiments indicate that the perception of number is interconnected to the perception of time and space intervals [75].

The overall bottom line is that even in the XXZ quantum network the emerging dynamical frequencies - or else the numerosity counting itself- comes from the number of consecutive gaps between the original levels. In fact, up to perturbative levels, anisotropy is found to just inject an uncertainty due to degeneracy lifting and leading to consequent spreading of the bands, the latter depending itself on the number of excitations introduced.

With this physical understanding at hand, we can now turn our attention to the transport properties of more general quantum networks, where we release either the constraint of constant coupling intensity of the links in the regular network, or the regular architecture itself by considering complex quantum networks. This is the subject of the next Section 3, where we explore the extent to which the space and time memory-preserving property of the regular- XXZ network excitations can be engineered in more general networks.

3 Transport properties in generalized quantum networks

So far we have exploited the concept of cooperative shielding to build intuition and theoretical understanding about the out-of-equilibrium dynamical behavior of the closed quantum spin network governed by the XXZ Hamiltonian, for a network with all-to-all connectivity architecture of equally weighted links. For this case, we could resort to semi-analytical means. In this section, we start from

the understanding developed in Section 2 to numerically investigate the role played by the interaction graph in a complex quantum system architecture. For simplicity, we stick to case of one single excitation, having developed in Section 2 an intuition for multiple excitations: we will come back to this point in the concluding Section 4. As an example for complex quantum network we choose the small-world architecture: besides being *per se* relevant for diverse problems, we are here interested to its property of well interpolating between the cases of regular and random graphs after tuning only two parameters. We analyze the underlying physics by specializing our analysis to two relevant quantities, a localization quantifier called Inverse Participation Ratio (IPR) (see Appendix 1) and the relative distance Δ_{IPR} introduced to measure how much the IPRs of the small-world graphs depart from the all-to-all networks (see below).

3.1   Small-world networks

A number of real-life networks relevant to diverse phenomena, ranging from biology to social sciences, are characterized by a high level of clustering and, at the same time, by a low average distance between the vertices: this is the so-called "small-world phenomenon" that illustrates e.g. social networks and the World Wide Web [76].

Such a network can be built from a regular-lattice graph where each node is linked to its first $2k$ neighbors, and then introducing a rewiring probability β that one edge connects the starting node to a different one. The parameter $2k$ drives the degree of network complexity. The parameter β governs the level of graph's randomness, bridging between the regular-lattice case with $\beta = 0$ and the fully random graph with $\beta = 1$. The all-to-all connected graph is obtained in the limit $\beta = 0$ and $2k/(L-1) = 1$. The construction mechanism is illustrated in Fig. 4(a).

We complete this introductory section by recalling the main qualifiers and quantifiers for the networks architectures considered in complex-network theory, that will be used in the following. For details, we refer to the Appendix. One first connectivity quantifier is the network's degree, that is the number of edges linking one node to others. The coupling range is quantified by the topological distance dist_{ij}, counting the number of links connecting two sites in their shortest path: a global distance quantifier $\mathcal{D}$ can then be usefully introduced, as the average of the topological distance over all the pairs of nodes. Finally, the tendency to aggregate is quantified by the clustering $\mathcal{C}$, that is the average proportion of total triangles (meaning closed loops of three vertices) within a given neighborhood, as related to the maximum number of allowed connections according to the local degree. All-to-all connected graphs are the limiting case of low topological distance, i.e. tending to 1, and high clustering coefficient, i.e. tending to 1; in the opposite limiting case of nearest-neighbor networks both local and global clustering are 0, since no triangles between nodes can be observed, while average distance linearly scales as the number of sites L.
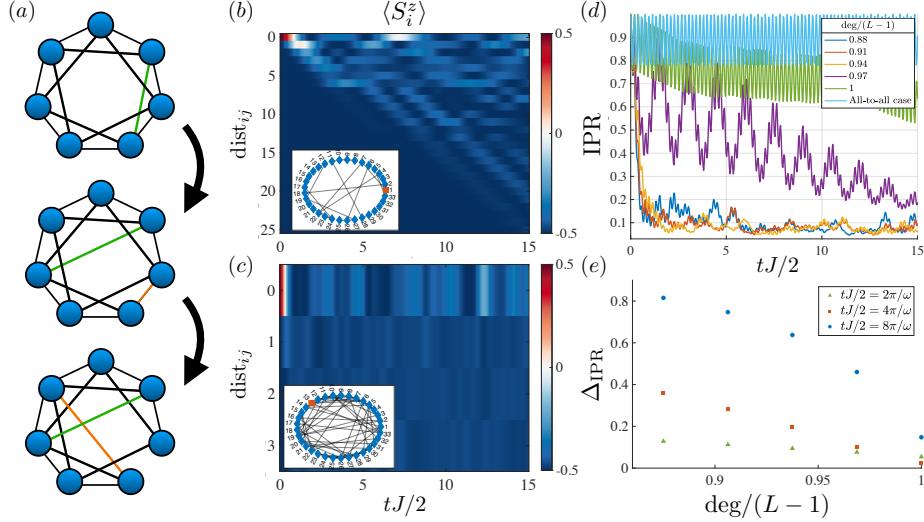
15

Figure 4: Construction of small-world graphs and their transport properties. (a) Small-world network construction (see text). Top to bottom: a regular graph with $L = 7$ sites and $k = 2$ nearest-neighbor connections, and different rewired links (green and orange) with respect to the original graph, according to the value of the probability β. $(b) - (c)$ Examples of transport for one quenched excitation along the z-axis in two different networks with $L = 33$ sites, shown in the corresponding insets with the initial site highlighted in red (sub-figure (b) has initial $k = 1$ and initial site 1 with degree 1, while (c) has $k = 3$ and initial site 13 with degree 6). The average local z-magnetization $\langle \hat{\mathcal{S}}_i^z \rangle$ time signal is displayed as a function of the dimensionless time $tJ/2$ (horizontal axis), in sites (vertical axis) having the same topological distance dist_{ij} from the site where the excitation has been injected. (d) Time evolution of the Inverse Participation Ratio (IPR) for one excitation injected in different initial sites of a network with small rewiring probability β and large k values, for the different connectivity levels in the legend as measured by the values of the degree, i.e. the number of edges, related to $(L-1)$: values closer to 1 tend towards an all-to-all connected graph (light-blue curve). Parameters: $L = 33$, $2k = L - 2$, $\beta = 0.1$. (e) IPR distance (12) between all-to-all and small-world networks graphs as a function of the initial site's degree related to $L - 1$ at increasing times as in the legend.

3.2   Inverse Participation Ratio

The transport properties of one excitation in such networks can be characterized by means of a de-localization quantifier, the Inverse Participation Ratio (IPR)

$$\text{IPR}(t) = \sum_s \langle s | \hat{\varrho}(t) | s \rangle^2 ,$$

16

defined as the sum of the squared trace elements of the density matrix $\hat{\varrho}$ over single-excitation localized states $\{|s\rangle\} = \{|\downarrow\downarrow \ldots \downarrow\uparrow\downarrow \ldots \downarrow\rangle\}$, where the $\uparrow$ in the previous Pauli string is a spin up (along z) located at site s; this basis has dimension L and constitutes one of the subspaces of the total z-magnetization operator $\hat{\mathcal{M}}_z$ with which $\hat{\mathcal{H}}$ can be block-diagonalized. While we refer to the Appendix for a complete definition, we here highlight that by definition the IPR values range from $1/L$ for the complete delocalized state, i.e. infinite-temperature case, to 1 for the perfect localization on a single eigenstate. If needed, generalizations of this quantifiers to the case of multiple excitations can be introduced, as in [4].

We begin by examining the rate of local transport in Fig. 4$(b - c)$ showing two examples for the time-evolution of the local z-magnetization signals according to different values of the topological distance dist_{ij} for two different degrees of connectivity. We observe that in the sparsely connected case (b) the initial excitation takes longer time to spread across the network with respect to more connected case (c), leading to the clear emergence of a light-cone for the spreading of the excitation. As the number of connections increases (c), the de-localization of the first excitation is distributed between all sites more or less evenly: therefore, the spreading occurs at very short times with and the cone structure is harder to identify. Thus, it is interesting to study increasing connectivities close to the limit of all-to-all connected networks. The results are illustrated in Fig. 4(d), where we consider a network with a given $k = L - 2$ parameter, closest to all-to-all case but not-fully connected, and impose a non-zero rewiring probability providing the sites with different degrees, i.e. different number of links with other elements. Then, we compute the IPR by picking different initial sites according to their degree. We observe that the IPR time-evolution behavior for the all-to-all case soon breaks into the general small-world system behavior. Here, the degeneracy lifting due to the symmetry reduction makes the IPR decreasing over time towards full delocalization (yellow, orange, and dark blue curves), instead of oscillating around the localization condition (light blue and green curves). We notice the intermediate case displayed by the purple curve, that seems to herald the passage from localization to delocalization with IPR oscillations that increase in amplitude and slow down in time.

We quantity the departure of small-world behavior from the all-to-all connectivity case in Fig. 4(d), where we introduce an indicator for the difference the distance:

$$\Delta_{\text{IPR}}(t) = \frac{|\text{IPR}_{\text{a.a.}}(t) - \text{IPR}_{\text{s.w.}}(t)|}{\text{IPR}_{\text{a.a.}}(t)}. \tag{12}$$

Different dots colors for Δ_{IPR} refer to values computed at different time instants $tJ/2$ in units of $2\pi/\omega$, ω being determined as in Eq. 3 for the quantum numbers $l = L/2$ and $m = -L/2 + 1$. Each point represents the average computed over initial sites having the same degree in the same network as in Fig. 4(d). As expected, we observe an increasing difference while the network's degree departs from $L-1$ (degree/$(L-1) < 1$) corresponding to all-to-all connectivity, the difference being enhanced at each degree value with increasing time.

17

While these results are intuitively sound, as in Section 2 we search for analytical understanding. Since the analytical machinery that we established for regular networks seems to not apply for irregular graphs, we seek for alternatives. It turns out that this is possible at least for the short-time IPR behavior, by means of the so-called cascade model introduced in [77]: in essence, this monitors the initial state $|s(0)\rangle$ coupling with other basis elements at different moments $|s(t)\rangle$.

The underlying idea is as follows, see Fig. 5(a) for the concept. At $t = 0$, only the subset of state vectors $\mathcal{F}_0$ containing $|s\rangle$ participates in the temporal evolution. Immediately after, to first-order approximation the temporal evolution operator connects the initial state to the basis vectors $|f_i\rangle$ for which the matrix elements $\langle f_i|\hat{\mathcal{H}}|s\rangle$ are non-vanishing, thus extending the subset of involved states to $\mathcal{F}_1$. More precisely, the subset of states grows as

$$\mathcal{F}_0 = \{|s\rangle\} \xrightarrow{\exp{(\mathrm{i}\hat{\mathcal{H}}t)} \simeq (\hat{\mathbb{1}} - \mathrm{i}\hat{\mathcal{H}}t)} \mathcal{F}_1 = \{|s\rangle\} \cup \{|f_i\rangle, \ f_i \text{ first neighbors of } s\}. \quad (13)$$

In fact, one can set and resolve rate equations for the probabilities of finding the state evolution $|s(t)\rangle$ to a particular basis element $|f_i\rangle$:

$$P_{f_i}(t) = |\langle f_i|s(t)\rangle|^2.$$

Borgonovi et al. have found a transparent expression for the evolution of IPR at short times, in the approximation where any back-flow to the initial site can be neglected [77]. This is:

$$\mathrm{IPR}(t) \approx P_s^2 + \frac{\sum_{f_i} P_{f_i}^2}{\mathcal{N}_1}, \quad (14)$$

where the sum is performed over the first-neighbor sites of the initial one, and $\mathcal{N}_1$ is the number of such nodes plus one (referring to vertex s). Let us better understand eq. 14: as the survival probability P_s decreases because of the excitation spreading, the initial site couples with its first neighbors in the interaction topology. In other words, the IPR evolution is strictly dependent on the graph upon which it lives, through its adjacency matrix A_{ij} describing the existing connections and being proportional to the XX Hamiltonian itself, when written in the restricted basis of Pauli vectors having one excitation. Notice that $A_{ij} = 1$ if sites i and j are linked, else $A_{ij} = 0$. Under a different perspective, the degree of the initial node (i.e. the number of first neighbors in the graph) governs the transport onset at short times.

This procedure can easily be generalized to later times. Indeed, as we go further, the powers of $\hat{\mathcal{H}}$ participate to the initial state evolution. Since $\hat{\mathcal{H}}$ is proportional to the adjacency matrix, elevating the latter to a certain power p tells us the topological distance between two sites if it is less than p, i.e. it refers to the subset of states contributing to the time propagation.

A summary of the analytical results is presented in Fig. 5. In Fig. 5(b) − (c), we compare the simulated (blue curves) IPR time behavior with the predictions
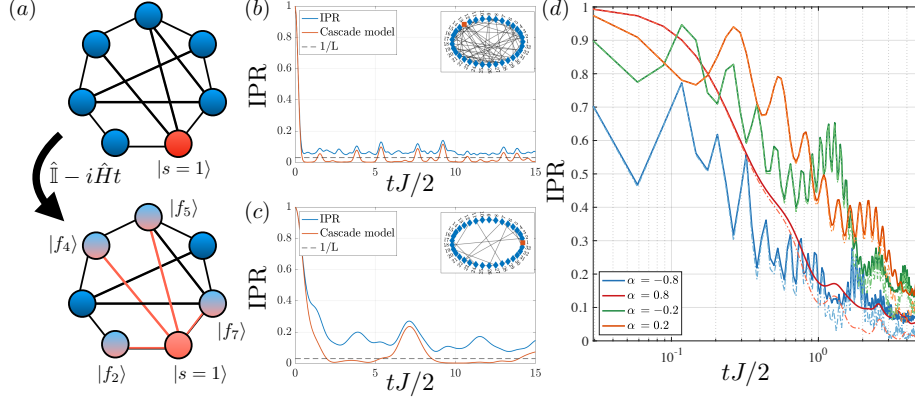
Figure 5: Understanding transport in highly-connected graphs at early times. (a) Concept of the cascade model (see text). Top: an initial excitation (red circle) in a generic network (black edges) is located at site 1, as denoted by the state $|s = 1\rangle = |\uparrow\downarrow \ldots \downarrow\rangle$ and the red circle opposed to the blue ones. Bottom: after a short temporal evolution (black arrow) the initial excitation has spread (gradient-colored circles) across site 1's first neighbors (orange edges), such that the state is a superposition of $|s = 1\rangle$ and states $|f_2\rangle = |\downarrow\uparrow\downarrow \ldots \downarrow\rangle$, $|f_4\rangle$, $|f_5\rangle$ and $|f_7\rangle$. (b) − (c) Comparison of the IPR's time evolution as computed from the cascade model (orange curves) and from a numerical simulation (blue curves) for the small-world network depicted in the inset with $L = 33$ nodes and excitation injected in different sites (red dot). The complete delocalization limit $1/L$ is shown with a dashed line. (b) Case with low average distance between sites (network parameters: $k = 1, \beta = 0.31$). (c) Case with large average distance between sites (network parameters: $k = 2, \beta = 0.88$). (d) IPR early-time evolution for a fully-connected network with $L = 33$ nodes and links intensity that changes with physical distance according to a power law with coefficient α as in the legend, $J_{ij} \propto \text{dist}(i, j)^{-\alpha}$, where $\text{dist}(i, j) = \min(|i - j|, L - |i - j|)$ for the PBCs considered in all these cases. The predictions of the cascade model for the corresponding α are represented with same colors, but dashed lines.

of the cascade model (orange curves) for two complex network graphs that are highly (b) and sparsely (c) connected, respectively. For earlier times we find a good agreement between the IPR simulations and the predictions provided by the cascade model. In fact, this is able to predict the sharp deviation from the all-to-all case, heralding the breaking of the spectral degeneracy and the halt of cooperative shielding. The later times behavior from the cascade model misses the bumps that are likely due to the backflow processes, that are neglected in the model approximations.

A different way to break space regularity in networks is to consider exchange coupling that vary with physical distance, specifically characterized by a power

law, i.e. $J_{ij} \propto \text{dist}(i,j)^{-\alpha}$ in Eq. (1) which in the case of PBCs is equivalent to $\min(|i-j|, L-|i-j|)$. We thus take advantage of the cascade model to check on the excitation localization properties for this topology setting. This is illustrated in Fig. 5(d), where we compare the cascade model with the IPR evolution at early times for two distinct values of $|\alpha|$. We observe good agreement until $tJ/2$ times corresponding to the tunneling time to second neighbors. The regular lattice with variable distance coupling soon deviates from the all-to-all graph, the cascade model accurately predicting this deviation. Overall then, we can conclude that space regularity, at least on a local scale and already at early times, is paramount for the emergence of highly-degenerate eigenspaces that induce the trapping of excitations via cooperative shielding. Therefore, any deviation from such space regularity soon leads to delocalization of injected excitations. The question then arises about what happens on a global scale.

We thus turn on investigating the IPR for graphs highly connected on a global scale, after tuning the tendency to clusterize and the rewiring probability. In so doing, we aim to check whether a parameter's range exists, for which the memory-preserving property remains protected for a significant space and temporal window. Therefore, we now revert back to simulations performed over longer-enough temporal windows, so that information or energy has spread throughout the network, to evaluate the participation of the basis vectors to the initial state's temporal evolution (given by its inverse). To explore the whole physics landscape, we now simulate a set of 10 graphs with size $L = 33$, for each pair of generative parameters (k, β) with $k = 1, 2, \ldots, 15$ (maximum possible $k = 16$, equivalent to the all-to-all situation) and $\beta = 0.1, 0.2, \ldots, 1$. For each case study, we take the average value of the IPR in a temporal window chosen such that the excitation could have the time to travel across the whole graph: specifically, we simulate the temporal evolution for the period $tJ/2 \in [0, 100]$ and compute the average for times in the interval $tJ/2 \in [90, 100]$. Then, for each given pair (k, β) we compute the average of the provided time averages for each graph.

We summarize the results in Fig. 6. The boxplot displays the average IPR as a function of the number of initial neighbors $2k$, for different values of the rewiring probability β. We see that localization, i.e. higher IPR values, is favored for extremal values of k (1 and 15). The lower extreme corresponds to the obvious case of low connectivity, specifically similar to a nearest-neighbor connection. The latter, instead, corresponds to the case of highly connected graphs with significant interference effects. Delocalization manifests instead at intermediate connectivity conditions. The rewiring probability β does not significantly influence the average value, essentially dominated by the number of neighbors. We associate variations in this behavior with the limited number of sampled graphs.

We now represent in Fig. 6(b) the same IPR results in a scatter plot where the graphs are characterized by their average distance and average clustering (see Appendix) instead. We see that relatively localized long-time states are possible away from the limit of all-to-all connected graphs, that is with average clustering and average distance equal to 1. Quite interestingly, non-trivial steady states

emerge not only in the highly connected cases but also in sparsely connected graphs with high-average distance, due to the slow propagation of excitation and small interference. This behavior heralds the potential for a memory-preserving property of the initial quench even away from the all-to-all case, should a certain decoding protocol be provided. In contrast, with k values large compared to an all-to-all case with $L(L-1)/2$ (see orange arrow), signatures of cooperative shielding appear, typical of complete connection. The difference between the finite IPR values (green to light-blue symbols) shown in the top-left and in the bottom-right part of Fig. 6(b) is better envisioned by inspecting Fig. 6(c). Here we show a typical IPR vs. time $tJ/2$ behavior (blue line) for parameter values in the bottom-right part of (b). The IPR signal oscillates around an average that is clearly above the threshold $1/L$ of complete delocalization, though the average value is lower and irregular with respect to the IPR in a corresponding all-to-all case (yellow). The cascade model prediction (red) only provides a good fit at short times. This is due to the fact that the cascade model neglects all backflow processes. Thus, we might infer that the emerging localization in this region is enhanced by quantum interference effects among different paths, in a mechanism similar to Anderson localization [78].

4 Discussion and conclusions

This work is motivated by the relevance of complex quantum networks in the modeling of biological systems and as powerful tools to extract from many-body systems relevant information connected to emerging entanglement properties or topological effects. We have therefore addressed the transport properties of quantum networks as governed by their connectivity graph and topology and by the range of the couplings connecting the nodes, properties that can be implemented in current quantum technology platforms [14]. We have focused on networks regulated by the XXZ Hamiltonian, that is a paradigmatic model with a variety of applications [72]. Motivated by the findings in [5], we have also focused on the property of spatial localization of initial quenches introduced in the network, and the robust preservation of their memory over long time, even in the out-of-equilibrium quantum network, irrespective of where and when the excitations are switched on, and of their number. This peculiar phenomenon essentially results into a spatiotopic representation of the number of frequencies in the power spectrum of the network, that are as many as the number of excitations initially injected. Conversely, the power spectrum maps the space and time location of the initial excitations. Even more interestingly, the uncertainty in the number of excitations that the quantum network can map, linearly increases with the number itself. This behavior is shown in [5] to elegantly account for the so-called Weber's law for numerosity perception in neuroscience problems, after mapping the essential functions of the classical neuronal network into an open quantum network (resulting into the XXZ model), and in contrast with the poor performance of conventional biologically inspired models like artificial neural networks. In fact, this memory preserving property can be of much
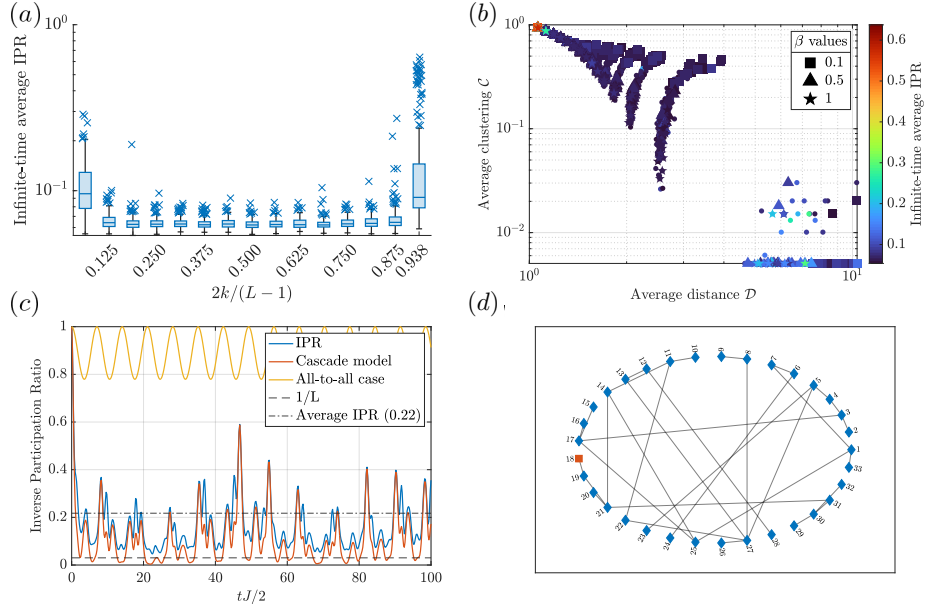
21

Figure 6: Effect of network topology on the long-time average IPR. For each pair (k, β) of initial conditions in the graph generation, the computed average IPR in the time window $tJ/2 \in [90, 100]$, to ensure that the excitation could travel across the whole graph. (a) Long-time averaged IPR vs. the number of initial neighbors $2k$ normalized to $L-1$. Each $2k/(L-1)$ value represents the median (horizontal bar inside the boxes) or quartiles and outliers (crosses). Localization is seen to occur at extremal values of k, i.e. nearest-neighbor and all-to-all type of connectivity. Parameter values: $k = 1, \ldots, 15$, $\beta = 0.1, 0.2, \ldots, 1$, $L = 33$, 20 samples for each couple (k, β). (b) Long-time averaged IPR in the form of a scatter plot in the parameter space of average clustering $\mathcal{C}$ and average distance $\mathcal{D}$. The arrow indicates increasing values of k. Notice that, away from all-to-all connectivity with $\mathcal{C} = \mathcal{D} = 1$, some degree of localization is still possible for more regular networks, i.e. sparse graphs with large $\mathcal{D}$ and intermediate to very low values of clustering $\mathcal{C}$. We see this in panel (c) showing a typical graph of IPR vs. dimensionless time $tJ/2$ (blue line) for parameter values $k = 1, \beta = 0.5, \mathcal{D} = 4.8, \mathcal{C} = 0$ in the bottom-right part of (b), corresponding to the network in (d) initialized at site 18, as depicted. The IPR displays irregular oscillations around an average (dot-dashed line) that is well above the threshold $1/L$ of complete delocalization (dashed line). For comparison, the IPR signal is shown for the all-to-all case (yellow) and from the cascade model (red).

interest for concrete implementations with current quantum technologies.

To gain insights on this complex matter, we have adopted a methodology that progressively develops understanding from the simpler to harder cases: we start from the all-to-all connectivity with constant coupling among the nodes,

then introducing power-law interactions in the regular network, and eventually passing to irregular, complex networks. The methodology employes combined analytical and numerical methods, revolving around the cooperative shielding concept and quantum cascade model [69] accompanied by exact diagonalization.

Three main results emerge from our analysis. First, the memory preserving properties of the all-to-all connected network have been traced back to the symmetry structure of the Hamiltonian via the concept of cooperative shielding. Both the one-to-one correspondence of the number of excitations with the number of frequencies in the power spectrum and the number uncertainty have been analytically explained, the former as a consequence of the Wigner-Eckart theorem to get the allowed quantum numbers from the usual angular momentum composition rules. In any event, employing different quantifiers in conjunction with IPR would certainly be a best suited strategy for a thorough characterization of quantum information transport, including e.g. entanglement entropy or out-of-time ordered correlation functions.

Second, standing on the insight gained with all-to-all connectivity, but now predicting the early-time behavior with the cascade model, a similar understanding has been developed for irregular networks, by varying either the links strength according to a power law, or the network architecture via small world networks. Distinct IPR time-evolution behaviors can be observed as in Fig. 4(d), from complete localization to complete delocalization, also within individual nodes of a single complex network. The evolution between the two extremes deserves further systematic analytical and numerical investigation, to characterize its nature and explore its predictability.

Finally, our analysis leads to characterize the long-time behaviour of irregular networks to study signals of memory preservation of excitations, that is excitations that to some degree do not delocalize nor thermally relax. Quite interestingly indeed, this memory-preserving property emerges to be better protected not only in densely connected graphs close to all-to-all conditions but also in sparse and more irregular ones, i.e. with increasingly larger average distances and intermediate-to-low clustering conditions. While the average IPR value is lower and the time signal irregular with respect to the corresponding all-to-all case, effects from the initial quench are stronger in such regimes, likely due to smaller quantum interference effects. Overall, this memory-preserving property is seen to break already at short times, after introducing distance-dependent irregularities, either in the form of power-law changing links in a regular network or of large average distances among the nodes. However, we find parameter windows providing effective local regularity for the degeneracy to be protected at longer times and cooperative shielding be at work.

This work opens a number of interesting future directions. First, the case of more excitations initially injected is to be analyzed, though no significant surprises are to be expected [4, 5].

Second, it is known that the Weber's law in neuroscience holds as well for time and space intervals, provided they are above a certain threshold. Besides, in neuroscience it is experimentally known [75] that the perception of numbers and of time and space intervals are interconnected with each other, suggesting that

there is only one area of the brain dedicated to such an integrated mechanism. Based on a biomimicry argument, we therefore expect that similar properties can be encoded in our quantum XXZ network, envisioning how to concretely implement them in a quantum technology.

Third, the results in Fig. 6(b) suggest that the articulated behaviour of the complex quantum network might be more simply described through a universal behavior, according to one single parameter embodying all possible connectivity measures. More extended simulations and analysis can answer this question.

Acknowledgements

References

[1] Andrew J. Daley. "Twenty-five years of analogue quantum simulation". In: *Nature Reviews Physics* 5.12 (2023), pp. 702–703.

[2] M B Plenio and S F Huelga. "Dephasing-assisted transport: quantum networks and biomolecules". In: *New Journal of Physics* (2008). DOI: 10.1088/1367-2630/10/11/113019. URL: https://dx.doi.org/10.1088/1367-2630/10/11/113019.

[3] Diana A Chisholm et al. "Stochastic collision model approach to transport phenomena in quantum networks". In: *New Journal of Physics* 23.3 (Mar. 2021), p. 033031.

[4] Alessandro Civolani et al. "Engineering Transport via Collisional Noise: A Toolbox for Biology Systems". In: *Entropy* 26.1 (2024).

[5] Jorge Yago Malo et al. "Quantum spin models for numerosity perception". In: *PLOS ONE* 18.4 (Apr. 2023), pp. 1–16.

[6] Andrei Y. Khrennikov. *Ubiquitous Quantum Structure*. Springer Berlin Heidelberg, 2010. DOI: 10.1007/978-3-642-05101-2. URL: https://doi.org/10.1007%2F978-3-642-05101-2.

[7] Irina Basieva, Andrei Khrennikov, and Masanao Ozawa. "Quantum-like modeling in biology with open quantum systems and instruments". In: *Biosystems 201, 104328, 2021* (2020). DOI: https://doi.org/10.1016/j.biosystems.2020.104328. eprint: 2010.15573. URL: https://arxiv.org/pdf/2010.15573.pdf.

[8] Marc Andrew Valdez et al. "Quantifying Complexity in Quantum Phase Transitions via Mutual Information Complex Networks". In: *Phys. Rev. Lett.* 119 (22 Nov. 2017), p. 225301. DOI: 10.1103/PhysRevLett.119.225301. URL: https://link.aps.org/doi/10.1103/PhysRevLett.119.225301.

[9] S. Perseguers et al. "Quantum Critical Behavior of Entanglement in Lattice Bosons with Cavity-Mediated Long-Range Interactions". In: *Nature Physics* 6 (2010), p. 539. DOI: doi.org/10.1038/nphys1665.

[10] J. Nokkala et al. "Complex quantum networks as structured environments: engineering and probing". In: *Sci. Rep.* 6 (2016), p. 26861. DOI: doi.org/10.1038/srep26861.

[11] J Nokkala et al. "Reconfigurable optical implementation of quantum complex networks". In: *New Journal of Physics* 20.5 (May 2018), p. 053024. DOI: 10.1088/1367-2630/aabc77. URL: https://dx.doi.org/10.1088/1367-2630/aabc77.

[12] I. M. Georgescu, S. Ashhab, and Franco Nori. "Quantum simulation". In: *Rev. Mod. Phys.* (2014). DOI: 10.1103/RevModPhys.86.153. URL: https://link.aps.org/doi/10.1103/RevModPhys.86.153.

[13] Ehud Altman et al. "Quantum Simulators: Architectures and Opportunities". In: *PRX Quantum* 2 (1 Feb. 2021), p. 017003. DOI: 10.1103/PRXQuantum.2.017003. URL: https://link.aps.org/doi/10.1103/PRXQuantum.2.017003.

[14] Jorge Yago Malo et al. "Atomic Quantum Technologies for Quantum Matter and Fundamental Physics Applications". In: *Technologies* 12.5 (2024). ISSN: 2227-7080. DOI: 10.3390/technologies12050064. URL: https://www.mdpi.com/2227-7080/12/5/64.

[15] Andrew J. Daley. "Quantum trajectories and open many-body quantum systems". In: *Adv. Phys.* (2014). DOI: https://doi.org/10.1080/00018732.2014.933502. eprint: 1405.6694. URL: https://arxiv.org/pdf/1405.6694.pdf.

[16] W Hofstetter and T Qin. "Quantum simulation of strongly correlated condensed matter systems". In: *Journal of Physics B: Atomic, Molecular and Optical Physics* (2018). DOI: 10.1088/1361-6455/aaa31b.

[17] Christian W. Bauer et al. "Quantum simulation of fundamental particles and forces". In: *Nature Reviews Physics* 5.7 (2023), pp. 420–432.

[18] Luca Pezzè et al. "Quantum metrology with nonclassical states of atomic ensembles". In: *Rev. Mod. Phys.* (2018). DOI: 10.1103/RevModPhys.90.035005. URL: https://link.aps.org/doi/10.1103/RevModPhys.90.035005.

[19] J. Eisert, M. Cramer, and M.B. Plenio. "Area laws for the entanglement entropy - a review". In: *Rev. Mod. Phys.* (2010). DOI: https://doi.org/10.1103/RevModPhys.82.277. eprint: 0808.3773. URL: https://arxiv.org/pdf/0808.3773.pdf.

[20] F. Borgonovi et al. "Quantum chaos and thermalization in isolated systems of interacting particles". In: *Physics Reports* 626 (2016), pp. 1–58.

[21] Yudong Cao et al. "Quantum Chemistry in the Age of Quantum Computing". In: *Chemical Reviews* (2019). DOI: 10.1021/acs.chemrev.8b00803.

[22] Bela Bauer et al. "Quantum Algorithms for Quantum Chemistry and Quantum Materials Science". In: *Chemical Reviews* 120.22 (Nov. 2020), pp. 12685–12717.

[23] Jianshu Cao et al. "Quantum biology revisited". In: *Science Advances* (2020). DOI: 10.1126/sciadv.aaz4888. eprint: https://www.science.org/doi/pdf/10.1126/sciadv.aaz4888. URL: https://www.science.org/doi/abs/10.1126/sciadv.aaz4888.

[24] Jacob Biamonte, Mauro Faccin, and Manlio De Domenico. "Complex networks from classical to quantum". In: *Communications Physics* (2019). DOI: 10.1038/s42005-019-0152-6. URL: https://doi.org/10.1038/s42005-019-0152-6.

[25] Brian Swingle. "Unscrambling the physics of out-of-time-order correlators". In: *Nature Physics* (2018). DOI: 10.1038/s41567-018-0295-5. URL: https://doi.org/10.1038%2Fs41567-018-0295-5.

[26] Arpan Bhattacharyya, Lata Kh. Joshi, and Bhuvanesh Sundar. "Quantum information scrambling: from holography to quantum simulators". In: *The European Physical Journal C* (2022). DOI: 10.1140/epjc/s10052-022-10377-y. URL: https://doi.org/10.1140/epjc/s10052-022-10377-y.

[27] Gregory Bentsen, Yingfei Gu, and Andrew Lucas. "Fast scrambling on sparse graphs". In: *Proceedings of the National Academy of Sciences* (2019). DOI: 10.1073/pnas.1811033116. eprint: https://www.pnas.org/doi/pdf/10.1073/pnas.1811033116. URL: https://www.pnas.org/doi/abs/10.1073/pnas.1811033116.

[28] Supriyo Datta. *Quantum Transport: Atom to Transistor*. Cambridge University Press, 2005. DOI: 10.1017/CBO9781139164313.

[29] Colin John Lambert. *Quantum Transport in Nanostructures and Molecules*. 2053-2563. IOP Publishing, 2021.

[30] Graham R. Fleming, Gregory D. Scholes, and Yuan-Chung Cheng. "Quantum effects in biology". In: *Procedia Chemistry* 3.1 (2011), pp. 38–57.

[31] Reka Albert and Albert-Laszlo Barabasi. "Statistical mechanics of complex networks". In: *Reviews of Modern Physics* (2002). DOI: 10.1103/RevModPhys.74.47. eprint: cond-mat/0106096. URL: https://arxiv.org/pdf/cond-mat/0106096.pdf.

[32] Philip Ball. "Physics of life: The dawn of quantum biology". In: *Nature* (2011). DOI: 10.1038/474272a. URL: https://doi.org/10.1038/474272a.

[33] S.F. Huelga and M.B. Plenio. "Vibrations, quanta and biology". In: *Contemporary Physics* (2013). DOI: 10.1080/00405000.2013.829687. eprint: https://doi.org/10.1080/00405000.2013.829687. URL: https://doi.org/10.1080/00405000.2013.829687.

[34] Gabor Vattay, Stuart Kauffman, and Samuli Niiranen. "Quantum Biology on the Edge of Quantum Chaos". In: *PLOS ONE* (2014). DOI: 10.1371/journal.pone.0089017. URL: https://doi.org/10.1371/journal.pone.0089017.

[35] Nikolaj Kulvelis, Maxim Dolgushev, and Oliver Mülken. "Universality at Breakdown of Quantum Transport on Complex Networks". In: *Phys. Rev. Lett.* 115 (12 Sept. 2015), p. 120602. DOI: 10.1103/PhysRevLett.115.120602. URL: https://link.aps.org/doi/10.1103/PhysRevLett.115.120602.

[36] Oliver Mülken, Maxim Dolgushev, and Mircea Galiceanu. "Complex quantum networks: From universal breakdown to optimal transport". In: *Phys. Rev. E* (2016). DOI: 10.1103/PhysRevE.93.022304. URL: https://link.aps.org/doi/10.1103/PhysRevE.93.022304.

[37] Sigmund Kohler, Jörg Lehmann, and Peter Hänggi. "Driven quantum transport on the nanoscale". In: *Physics Reports* 406.6 (2005), pp. 379–443.

[38] Manuel Alamo, Francesco Petiziol, and André Eckardt. "Minimal quantum heat pump based on high-frequency driving and non-Markovianity". In: *Phys. Rev. E* 109 (6 June 2024), p. 064121. DOI: 10.1103/PhysRevE.109.064121. URL: https://link.aps.org/doi/10.1103/PhysRevE.109.064121.

[39] Jeremy M Moix, Michael Khasin, and Jianshu Cao. "Coherent quantum transport in disordered systems: I. The influence of dephasing on the transport properties and absorption spectra on one-dimensional systems". In: *New Journal of Physics* 15.8 (Aug. 2013), p. 085010.

[40] Mattia Walschaers et al. "Quantum Transport on Disordered and Noisy Networks: An Interplay of Structural Complexity and Uncertainty". In: *Annual Review of Condensed Matter Physics* 7.Volume 7, 2016 (2016), pp. 223–248.

[41] Chenyi Zhou, Xiaobin Chen, and Hong Guo. "Theory of quantum transport in disordered systems driven by voltage pulse". In: *Phys. Rev. B* 94 (7 Aug. 2016), p. 075426. DOI: 10.1103/PhysRevB.94.075426. URL: https://link.aps.org/doi/10.1103/PhysRevB.94.075426.

[42] Ling-Na Wu and André Eckardt. "Heat transport in an optical lattice via Markovian feedback control". In: *New Journal of Physics* 24.12 (Dec. 2022), p. 123015.

[43] Benedikt Kloss and Yevgeny Bar Lev. "Spin transport in disordered long-range interacting spin chain". In: *Phys. Rev. B* 102 (6 Aug. 2020), p. 060201. DOI: 10.1103/PhysRevB.102.060201. URL: https://link.aps.org/doi/10.1103/PhysRevB.102.060201.

[44] G. A. Domínguez-Castro and R. Paredes. "Enhanced transport of two interacting quantum walkers in a one-dimensional quasicrystal with power-law hopping". In: *Phys. Rev. A* 104 (3 Sept. 2021), p. 033306. DOI: 10.1103/PhysRevA.104.033306. URL: https://link.aps.org/doi/10.1103/PhysRevA.104.033306.

[45] Nicolò Defenu et al. "Long-range interacting quantum systems". In: *Rev. Mod. Phys.* 95 (3 Aug. 2023), p. 035002. DOI: 10.1103/RevModPhys.95.035002. URL: https://link.aps.org/doi/10.1103/RevModPhys.95.035002.

[46] Colin D. Bruzewicz et al. "Trapped-ion quantum computing: Progress and challenges". In: *Applied Physics Reviews* 6.2 (May 2019), p. 021314.

[47] Helmut Ritsch et al. "Cold atoms in cavity-generated dynamical optical potentials". In: *Rev. Mod. Phys.* 85 (2 Apr. 2013), pp. 553–601. DOI: 10.1103/RevModPhys.85.553. URL: https://link.aps.org/doi/10.1103/RevModPhys.85.553.

[48] C S Adams, J D Pritchard, and J P Shaffer. "Rydberg atom quantum technologies". In: *Journal of Physics B: Atomic, Molecular and Optical Physics* 53.1 (Dec. 2019), p. 012002.

[49] Lauriane Chomaz et al. "Dipolar physics: a review of experiments with magnetic quantum gases". In: *Reports on Progress in Physics* 86.2 (Dec. 2022), p. 026401.

[50] R. Botet, R. Jullien, and P. Pfeuty. "Size Scaling for Infinitely Coordinated Systems". In: *Phys. Rev. Lett.* 49 (7 Aug. 1982), pp. 478–481. DOI: 10.1103/PhysRevLett.49.478. URL: https://link.aps.org/doi/10.1103/PhysRevLett.49.478.

[51] F. Liu et al. "Confined Quasiparticle Dynamics in Long-Range Interacting Quantum Spin Chains". In: *Phys. Rev. Lett.* 122 (15 Apr. 2019), p. 150601. DOI: 10.1103/PhysRevLett.122.150601. URL: https://link.aps.org/doi/10.1103/PhysRevLett.122.150601.

[52]   N. Defenu et al. "Dynamical Critical Scaling of Long-Range Interacting Quantum Magnets". In: *Phys. Rev. Lett.* 121 (24 Dec. 2018), p. 240403. DOI: 10.1103/PhysRevLett.121.240403. URL: https://link.aps.org/doi/10.1103/PhysRevLett.121.240403.

[53]   A. Campa, T. Dauxois, and S. Ruffo. "Statistical mechanics and dynamics of solvable models with long-range interactions". In: *Physics Reports* 480.3 (2009), pp. 57–159. ISSN: 0370-1573. DOI: https://doi.org/10.1016/j.physrep.2009.07.001. URL: https://www.sciencedirect.com/science/article/pii/S0370157309001586.

[54]   M. F. Maghrebi, Z.-X. Gong, and A. V. Gorshkov. "Continuous Symmetry Breaking in 1D Long-Range Interacting Quantum Systems". In: *Phys. Rev. Lett.* 119 (2 July 2017), p. 023001. DOI: 10.1103/PhysRevLett.119.023001. URL: https://link.aps.org/doi/10.1103/PhysRevLett.119.023001.

[55]   G. Giachetti et al. "Berezinskii-Kosterlitz-Thouless Phase Transitions with Long-Range Couplings". In: *Phys. Rev. Lett.* 127 (15 Oct. 2021), p. 156801. DOI: 10.1103/PhysRevLett.127.156801. URL: https://link.aps.org/doi/10.1103/PhysRevLett.127.156801.

[56]   R. Landig et al. "Quantum phases from competing short- and long-range interactions in an optical lattice". In: *Nature* 532.7600 (Apr. 2016), pp. 476–479. ISSN: 1476-4687. DOI: 10.1038/nature17409. URL: https://doi.org/10.1038/nature17409.

[57]   H. Habibian et al. "Bose-Glass Phases of Ultracold Atoms due to Cavity Backaction". In: *Phys. Rev. Lett.* 110 (7 Feb. 2013), p. 075304. DOI: 10.1103/PhysRevLett.110.075304. URL: https://link.aps.org/doi/10.1103/PhysRevLett.110.075304.

[58]   S. Sharma et al. "Quantum Critical Behavior of Entanglement in Lattice Bosons with Cavity-Mediated Long-Range Interactions". In: *Phys. Rev. Lett.* 129 (14 Sept. 2022), p. 143001. DOI: 10.1103/PhysRevLett.129.143001. URL: https://link.aps.org/doi/10.1103/PhysRevLett.129.143001.

[59]   T. Dauxois et al. *Dynamics and Thermodynamics of Systems with Long Range Interactions, Lect. Notes Phys. 602:1-19.* Springer Berlin, Heidelberg, 2002.

[60]   F. Borgonovi et al. "Broken Ergodicity in Classically Chaotic Spin Systems". In: *Journal of Statistical Physics* 116.5 (2004), pp. 1435–1447.

[61]   F. Borgonovi, G. L. Celardo, and G. P. Berman. "Quantum signatures of the classical topological nonconnectivity threshold". In: *Phys. Rev. B* 72 (22 Dec. 2005), p. 224416. DOI: 10.1103/PhysRevB.72.224416. URL: https://link.aps.org/doi/10.1103/PhysRevB.72.224416.

[62] Elliott H. Lieb and Derek W. Robinson. "The finite group velocity of quantum spin systems". In: *Communications in Mathematical Physics* (1972). DOI: 10.1007/BF01645779. URL: https://link.springer.com/content/pdf/10.1007/BF01645779.pdf.

[63] J. Schachenmayer et al. "Entanglement Growth in Quench Dynamics with Variable Range Interactions". In: *Phys. Rev. X* 3 (3 Sept. 2013), p. 031015. DOI: 10.1103/PhysRevX.3.031015. URL: https://link.aps.org/doi/10.1103/PhysRevX.3.031015.

[64] Jens Eisert et al. "Breakdown of Quasilocality in Long-Range Quantum Lattice Models". In: *Phys. Rev. Lett.* 111 (26 Dec. 2013), p. 260401. DOI: 10.1103/PhysRevLett.111.260401. URL: https://link.aps.org/doi/10.1103/PhysRevLett.111.260401.

[65] P. Hauke and L. Tagliacozzo. "Spread of Correlations in Long-Range Interacting Quantum Systems". In: *Phys. Rev. Lett.* 111 (20 Nov. 2013), p. 207202. DOI: 10.1103/PhysRevLett.111.207202. URL: https://link.aps.org/doi/10.1103/PhysRevLett.111.207202.

[66] Weitao Chen, Gabriel Lemarié, and Jiangbin Gong. "Critical dynamics of long-range quantum disordered systems". In: *Phys. Rev. E* 108 (5 Nov. 2023), p. 054127. DOI: 10.1103/PhysRevE.108.054127. URL: https://link.aps.org/doi/10.1103/PhysRevE.108.054127.

[67] A. G. Catalano et al. "Anomalous Diffusion in the Long-Range Haken-Strobl-Reineker Model". In: *Phys. Rev. Lett.* 131 (5 Aug. 2023), p. 053401. DOI: 10.1103/PhysRevLett.131.053401. URL: https://link.aps.org/doi/10.1103/PhysRevLett.131.053401.

[68] Antonio Sannia et al. *Skin effect in quantum neural networks*. 2024. arXiv: 2406.14112 [quant-ph]. URL: https://arxiv.org/abs/2406.14112.

[69] Lea F. Santos, Fausto Borgonovi, and Giuseppe Luca Celardo. "Cooperative Shielding in Many-Body Systems with Long-Range Interaction". In: *Phys. Rev. Lett.* (2016). DOI: 10.1103/PhysRevLett.116.250402. URL: https://link.aps.org/doi/10.1103/PhysRevLett.116.250402.

[70] David Burr and John Ross. "A Visual Sense of Number". In: *Current Biology* (2008). DOI: https://doi.org/10.1016/j.cub.2008.02.052. URL: https://www.sciencedirect.com/science/article/pii/S0960982208002388.

[71] Ivilin Stoianov and Marco Zorzi. "Emergence of a 'visual number sense' in hierarchical generative models". In: *Nature Neuroscience* (2012). DOI: 10.1038/nn.2996. URL: https://doi.org/10.1038/nn.2996.

[72] Fabio Franchini. *An Introduction to Integrable Techniques for One-Dimensional Quantum Systems*. Lecture Notes in Physics. http://dx.doi.org/10.1007/978-3-319-48487-7: Springer International Publishing, 2017.

[73] Sivaprasad Omanakuttan et al. "Scrambling and quantum chaos indicators from long-time properties of operator distributions". In: *Phys. Rev. A* (2023). DOI: [10.1103/PhysRevA.107.032418](https://link.aps.org/doi/10.1103/PhysRevA.107.032418). URL: https://link.aps.org/doi/10.1103/PhysRevA.107.032418.

[74] JJ Sakurai. *Modern Quantum Mechanics*. Addison-Wesley, 1994.

[75] D. Burr, A. Tozzi, and C. Morrone. "Neural mechanisms for timing visual events are spatially selective in real-world coordinates". In: *Nature Neuroscience* 10 (2007), p. 423. DOI: [doi.org/10.1038/nn1874](doi.org/10.1038/nn1874).

[76] Duncan J. Watts and Steven H. Strogatz. "Collective dynamics of 'small-world'networks". In: *Nature* (1998). DOI: [10.1038/30918](https://doi.org/10.1038/30918). URL: https://doi.org/10.1038/30918.

[77] Fausto Borgonovi, Felix M. Izrailev, and Lea F. Santos. "Exponentially fast dynamics of chaotic many-body systems". In: *Phys. Rev. E* (2019). DOI: [10.1103/PhysRevE.99.010101](https://link.aps.org/doi/10.1103/PhysRevE.99.010101). URL: https://link.aps.org/doi/10.1103/PhysRevE.99.010101.

[78] F Alet and N Laflorencie. "Many-body localization: An introduction and selected topics". In: *Comptes Rendus Physique* 19.6 (2018). Quantum simulation / Simulation quantique, pp. 498–525. ISSN: 1631-0705. DOI: [https://doi.org/10.1016/j.crhy.2018.03.003](https://www.sciencedirect.com/science/article/pii/S163107051830032X). URL: https://www.sciencedirect.com/science/article/pii/S163107051830032X.

Appendix

Inverse Participation Ratio

We provide here a compact description of the Inverse Participation Ratio (IPR), used as a quantifier of the (de)localization of an initial excitation. Given a density matrix $\hat{\varrho}(t)$ and the subspace of the L-dimensional Pauli basis $\mathcal{P}_1$ describing single-excitation localized states $\{|s\rangle\}$, the IPR is then the sum of $\hat{\varrho}$ trace elements squared:

$$\text{IPR}(t) = \sum_s \langle s|\hat{\varrho}(t)|s\rangle^2.$$

In the case where $\hat{\varrho}$ is a pure state, the IPR assumes the form:

$$|\psi(t)\rangle = \sum_s a_s(t)|s\rangle \implies \text{IPR}(t) = \sum_s |a_s(t)|^4.$$

The IPR is always comprised between $1/L$ and 1, corresponding to the limits of complete de-localization, i.e. infinite temperature case $\hat{\varrho} = \hat{\mathbb{1}}/L$, and perfect localization of the excitation in a state of our eigenbasis $|s_*\rangle$, respectively. Put it another way, the Participation Ratio (PR), which is the IPR's inverse, indicates how many elements of the chosen basis "significantly" participate to a pure state's temporal evolution, the lower meaning higher localization.

Characterizing complex graphs: average distance and clustering

We provide here the main definitions and relations for complex-networks properties quantifiers.

We first introduce the topological distance dist_{ij} between vertices i and j as the number of edges contained in their shortest path. The average distance $\mathcal{D}$ is its average over all possible couples:

$$\mathcal{D} = \frac{1}{\frac{L(L-1)}{2}} \sum_{i<j} \text{dist}_{ij} \,.$$

The clustering coefficient is instead a measure of the nodes' tendency to congregate. While there are many possible definitions, we refer to the one given by Watts and Strogatz in [76] since it is defined for the class of graphs we consider in this work, i.e. small-world networks. Specifically, it refers to the global clustering coefficient computed as average of the local ones. Given a node q with k_q neighbors (in other words it represents the degree of the site), we define the local clustering coefficient C_q as the proportion t_q of the number of triangles, i.e. the closed loops consisting of 3 nodes, containing q, counted with respect to the maximum number of allowed connections $k_q(k_q - 1)/2$ (if k_q is greater than 1): the latter is also referred in the literature as the overall amount of triplets, or subgraphs composed of three nodes connected with at least two edges. Using the properties of the graph's adjacency matrix A ($A_{ij} = 1$ if vertices i and j are connected, 0 otherwise), specifically the one that says that its powers indicate the number of walks between two sites, one can compute t_q as the matrix element $(A^3)_{qq}$ divided by 2 (graphs are undirected, so this allows to count the unique triangles). In summary, the clustering coefficient $\mathcal{C}$ comes as follows:

$$t_q = \frac{(A^3)_{qq}}{2} \implies C_q = \begin{cases} 0 & \text{if } k_q = 0,1 \\ t_q/[k_q(k_q - 1)/2] & \text{if } k_q > 1 \end{cases} \implies \mathcal{C} = \frac{1}{L} \sum_q C_q \,.$$

An intuition on this peculiar form of the clustering coefficient comes from social networks. Imagine a friendship group: your friends are generally friends between them. Besides, one of them can have a "long-distance connection" with another group. Such a link has the effect to reduce the level of assemblage of that association.

Let us make two limiting examples for a nearest-neighbor and completely-connected networks of size L. In the former case, $\mathcal{C}$ is 0 since the degree of each node is 2 hence no triangle can be formed, and $\mathcal{D}$ can be shown to scale linearly with L because the sum $\sum_{i<j} \text{dist}_{ij}$ can be written (L even, ring graph)

as:

$$\sum_{i<j} \text{dist}_{ij} = \underbrace{\left[1 + \cdots + \frac{L}{2} + \left(\frac{L}{2} - 1\right) + \cdots + 1\right]}_{\text{site } 1}$$

$$+ \underbrace{\left[1 + \cdots + \frac{L}{2} + \left(\frac{L}{2} - 1\right) + \cdots + 2\right]}_{\text{site } 2}$$

$$+ \ldots$$

$$+ \underbrace{[1]}_{\text{site } L},$$

which grows as L^3, while the total number of pairs as L^2. In the latter case, both $\mathcal{D}$ and $\mathcal{C}$ are 1, since every vertex is connected to the other by a link and all triplets turn out to be closed, thus becoming triangles.